

Triple-band polarization-insensitive wide-angle ultra-miniature metamaterial transmission line absorber

He-Xiu Xu,¹ Guang-Ming Wang,¹ Mei-Qing Qi,² Jian-Gang Liang,¹ Jian-Qiang Gong,³ and Zhi-Ming Xu⁴

¹Missile Institute, Air Force Engineering University, Xi'an 710051, Shaanxi, People's Republic of China

²State Key Laboratory of Millimeter Waves, Southeast University, Nanjing 210096, People's Republic of China

³National Key Laboratory of Antennas and Microwave Technology, Xidian University, Xi'an 710051, Shaanxi, People's Republic of China

⁴College of Science, Air Force Engineering University, Xi'an 710051, Shaanxi, People's Republic of China

(Received 4 July 2012; revised manuscript received 21 September 2012; published 5 November 2012)

We report on the design, fabrication, and measurement of a triple-band absorber enhanced from a planar two-dimensional artificial metamaterial transmission line (TL) concept. Unlike previous multiband absorbers, this implementation incorporates fractal geometry into the artificial TL framework. As a consequence of the formed large LC values, the utilized element is compact in size, which approaches $\lambda_0/15$ at the lowest fundamental resonant frequency. For independent control and design, a theoretical characterization based on a circuit model analysis (TL theory) is performed and a set of design procedures is also derived. Both numerical and experimental results have validated three strong absorption peaks across the S , C , and X bands, respectively, which are attributable to a series of self-resonances induced in the specific localized area. The absorber features near-unity absorption for a wide range of incident angles and polarization states and a great degree of design flexibility by manipulating the LC values in a straightforward way.

DOI: [10.1103/PhysRevB.86.205104](https://doi.org/10.1103/PhysRevB.86.205104)

PACS number(s): 78.20.Ci, 41.20.-q

I. INTRODUCTION

There has been considerable interest in using artificial electromagnetic (EM) metamaterials (MTMs) in the design of an absorber with nearly perfect absorption since Landy *et al.* proposed a perfect MTM absorber (MA) composed of electric resonators and cut wires.¹ Owing to the subwavelength element dimensions at the working wavelength, the MA overcomes traditional diffraction limits within an ultrathin substrate. In addition, MA also exhibits versatile distinct features over conventional material based absorbers such as flexible manipulation of the EM properties, a wide incident angle, polarization insensitivity, as well as nearly perfect absorptions. To date, large efforts and works have been devoted to this area, aiming to design an absorber exhibiting excellent performance within single-band,²⁻¹⁴ dual-band,¹⁵⁻²⁴ multiband,²⁵⁻³⁰ as well as broadband³¹⁻³⁵ operations. In light of explosive developments concerning EM MTMs, the concept of absorbers as one of the most promising applications of MTMs has undergone a great breakthrough during the past decade. The progress of the design has been demonstrated in almost every technologically relevant spectral range, extending significantly from the original microwave region^{1-5, 23-28, 31-34} to the terahertz region^{12-19, 29, 30} and even to the infrared and visible frequencies.^{6-11, 20-22, 35}

Although these absorbers can be tuned and optimized with comparably high absorptivity, polarization insensitivity, and wide angles of incidence, most of them are confined to the single-band and dual-band absorption response, and there is still a lack of sufficient progress toward the design and implementation of multiband (≥ 3) MAs. The current state of the art remarkably limits their potential applications in spectroscopic detection and phase imaging of hazardous materials and prohibited drugs which require distinct absorption features at multiple frequencies.¹⁹ Moreover, the available strategies to implement the flexible dual-band or multiband MAs are mostly

confined to the combinational approach, i.e., by combining two or more different resonant structures (electric resonators in essence) to form a new resonator,^{15-17, 22, 30} by incorporating a set of resonant geometries with aggressively scaled dimensions and appropriate distributions,^{18, 19, 25, 26} by placing identical resonant elements oriented in an orthogonal arrangement,^{20, 24} and by using multiple vertically stacked metallic layers.²⁸ Each resonator or layer couples separately to the electric components or magnetic components of the incident EM wave so as to absorb all the radiation completely at a specific resonant frequency. Although high flexibility is achieved, some of these absorbers may encounter two challenging issues which scientists and engineers should properly overcome: The former are element dimensions which are still unable to remain sufficiently small; the latter is the principle physics for a multiband MA which is still far from being well understood despite the introduction of a transmission line (TL) circuit model, which characterizes and interprets the mechanism of a single-band MA.³⁶ These drawbacks make the design and characterization of a multifunctional absorber a pressing task.

The goal of this paper is thus to propose an alternative strategy to acquire sufficiently smaller MTM elements and perform a comprehensive TL analysis on a triple-band absorber from a concept enhanced by a two-dimensional (2D) left handed (LH) TL (Ref. 37) which has more flexible reconfigurability. Therefore, the TL circuit model analysis is more straightforward than that presented in Ref. 36. The resultant absorber inherits almost all of the advantages of the MA such as nearly perfect absorption, and insensitivity to incident angles and polarization states. Most importantly, taking advantage of both the self-similarity and space-filling merits of the fractals, the fractal-perturbed element utilized to construct the absorber is considerably smaller because of the larger engineered semilumped circuit elements, and therefore it exhibits multifunctional self-resonant properties. Moreover, with the help of circuit model analysis, the resonant

frequencies can be manipulated with an arbitrary frequency ratio by adjusting the inductances and capacitances formed in specific localized current loops, enabling a real TL concept.

II. FUNDAMENTALS, THEORY, AND DESIGN

To begin, we first recall briefly some fundamentals and principle physics that have been established for metal-dielectric-metal MAs. To date, several theoretical approaches attempting to illustrate the underlying physics have been reported, including the excitation of the localized EM resonance,¹ TL circuit model analysis,³⁶ Fabry-Pérot resonance,³⁸ cavity resonance,³⁹ and interference theory.⁴⁰ Despite these progressive developments, this issue is still under debate. In this regard, we do not address this issue but focus on identifying a specific region associated with specific operating frequencies, which is the main concentration in this work and which is extremely essential for independent control and flexible design. Here, we will follow the mostly accepted absorption mechanism by relating multiband impedance matching to simultaneous electric and magnetic resonances and use the TL theory to further validate the specific localized resonances that have been drawn from the field analysis. It will be demonstrated that the conclusions drawn from these two approaches are reasonably consistent. These approaches are rational, based on the fundamental aspect that the proposed element is electrically very small, which enables the resulting periodical structure to be appropriately described as an effective bulk medium.

An absorber is typically composed of three functional layers which are constructed with a dielectric layer sandwiched between two metallic layers. The back layer is made of cut-wire MTM or a thick metallic plane, whereas the front layer is commonly made of periodically patterned metallic subwavelength electric resonators, coupling to the electric field (E -field) component of the incoming EM wave in the vicinity of the electric resonance. The antiparallel circulating currents between two metallic layers driven by the magnetic field (H field) are responsible for the magnetic resonance.¹ In order to maximize the absorptive efficiency characterized as $A(\omega) = 1 - T(\omega) - R(\omega)$, both the transmission, $T(\omega) = |S_{21}|^2$, and reflection, $R(\omega) = |S_{11}|^2$, should be minimized. The frequency-dependent effective permittivity $\varepsilon(\omega)$ and permeability $\mu(\omega)$ in the framework of an effective medium theory are formulated as $\varepsilon(\omega) = \varepsilon_1 + i\varepsilon_2$ and $\mu(\omega) = \mu_1 + i\mu_2$, respectively. Then the complex effective impedance $z(\omega) = z_1 + iz_2 = \sqrt{\mu(\omega)/\varepsilon(\omega)}$ and refractive index $n(\omega) = n_1 + in_2 = \sqrt{\mu(\omega)\varepsilon(\omega)}$ can be cautiously modulated with decent impedance matching at the air-MTM interface [$z(\omega) = 1$ and $R(\omega) = 0$]. Simultaneously, the transmission is null due to the shielding of the ground. Then all the power penetrating the MTM [$n_2 \rightarrow \infty$ and $T(\omega) = 0$] is completely consumed due to the ohmic and dielectric losses.¹⁴ Observation of these fundamentals illustrates that the electric and magnetic resonances play an essential role in the contribution of high-efficiency absorption and thus should be carefully conducted to enable them to share a center frequency.

As for the multiband absorber in the present design, $T(\omega)$ and $R(\omega)$ should approach to minimum simultaneously at several specific frequencies, around which several electric and

magnetic resonances are required. In essence, these resonances can be analyzed through a chain of cascaded LC resonant tanks corresponding to specific local regions. Figure 1 depicts the schematic as well as the equivalent circuit model of the proposed MTM element that was employed in the design of a triple-band absorber. As is clearly observed, the element particle is composed of three layers: a front 2D TL element which primarily responds to the E field and thus affords the electric resonances, a middle dielectric layer, and a back metallic ground plane. The front layer can be considered as a complete variation of the uniplanar LH TL element explored in Ref. 37, where a ring was loaded in each of its four corners as a series LH capacitor (lumped or distributed) and was connected to an adjacent ring through the gap via an LH inductor. The difference between the ring in this work and a previous one for a negative refractive index is that the ring here is constructed as quasi-Sierpinski space-filling curves of second iteration order⁴¹ from the point of view of a more compact unit cell and multiband behaviors. As a result, four subrings each with a self-inductance L_s are achieved. Moreover, four interdigital capacitors C_i are loaded at the middle of four concaves formed between the subrings, and two side meandered thin arms (3/2 fractal curves of first iteration order with length L) each with a self-inductance L_m are employed to connect the neighboring elements, with the aim of increasing the inductances and capacitances in a limited volume.

In addition to the aforementioned geometrical discrepancy, the most important aspect lies in a completely different operation mechanism for different applications from the one discussed in a previous article,³⁷ where a transverse electric (TE) wave is supported and the LH performance is a major concern. Moreover, the EM wave was horizontally incident (along the x axis) to the plane with the E field polarized along the y direction and the H field penetrating the structure plane, whereas in this work the absorber is illuminated under a normally incident EM wave [along the z axis; see Fig. 1(c)] with the polarization along either of two orthogonal directions in the plane because of nearly fourfold rotational symmetry (a fourfold rotation symmetry of the subrings and interdigitals while the meandered arms showed a left-and-right symmetry). Therefore, the E -field components drive the electric resonances of the LC circuits formed in different specific locations of the so-called 2D TL element (electric resonator) while the H -field components play a dominant role in driving the magnetic resonances of LC tanks formed in the corresponding positions between the metallic ground plane and the front TL element. Note that the fourfold rotational symmetry and the left-and-right symmetry of the meandered arms cannot be achieved at the same time. Moreover, the left-and-right asymmetric meandered arms will result in higher resonant frequencies of the TL element and, in turn, an electrically larger dimension due to the disconnection between adjacent cells which degrades the inductive effects to some degree.

The equivalent circuit model shown in Fig. 1(b) is proposed corresponding to three principle electric resonances on the assumption that the parasitic resonances of additional structures and the higher-order resonance of the interdigitals are negligible. A single port system is appropriate because

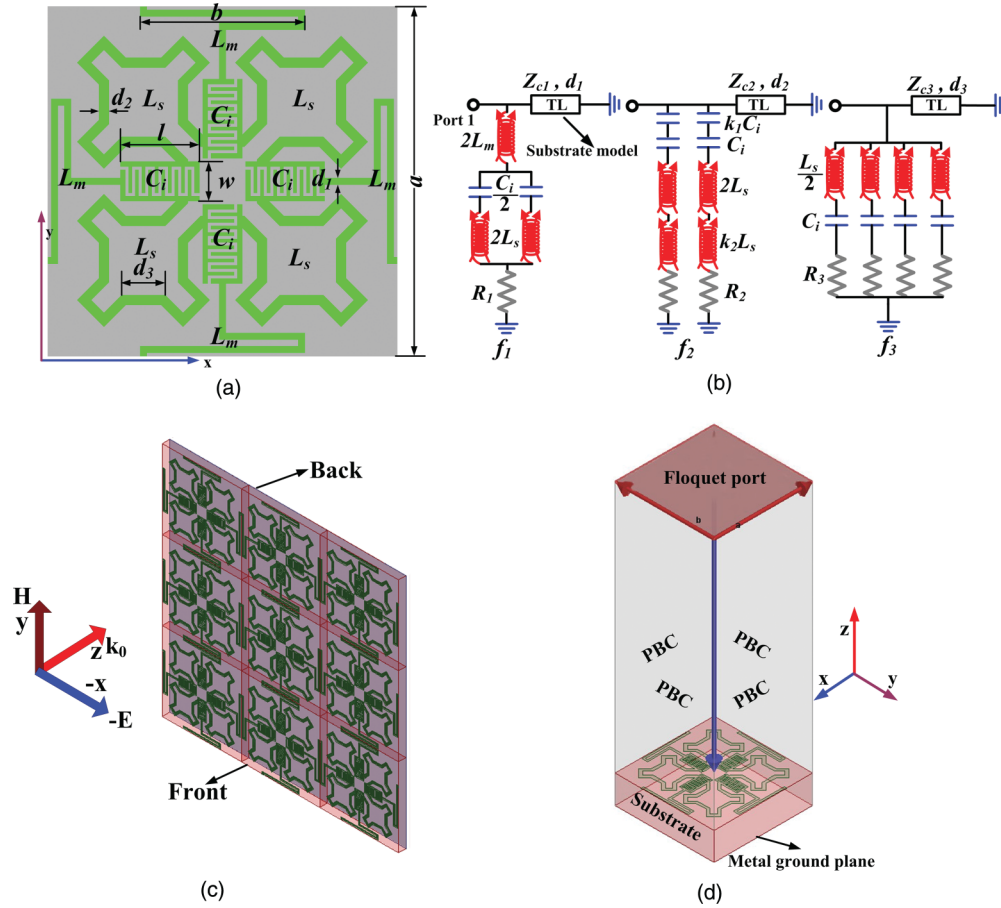


FIG. 1. (Color online) (a) Topology and (b) equivalent circuit models of the proposed MA structure at three principle resonances. (a) Top view of the MTM TL element. (b) Triple-circuit models corresponding to three individual resonances. (c) Respective view of a portion of the designed MA and (d) simulation setup in HFSS. The geometrical parameters (in mm) are listed as $a = 10.6$, $b = 5$, $l = 2.4$, $w = 1.2$, $d_1 = 0.2$, $d_2 = 0.3$, and $d_3 = 1.32$. The length of the meandered 3/2 fractal curve is $L = 6.8$.

the backside transmission is negligible.¹⁷ Here, the conventional TL section (also the LC circuit) with an equivalent impedance Z_{ci} and electrical length d_i incorporates not only the transmission through the dielectric substrate (with an impedance Z_0 and electrical thickness d_0) but also the localized magnetic resonant effects, whereas the back metallic layer is represented by ground. Notice that we combine these two parts in one TL section for convenience of analysis. The fundamental electric resonance of the front metal layer f_1 is induced by the two side inductors along the E -field direction, a parallel tank with each branch composed of two subring inductors, and two interdigital capacitors, yielding $f_1 = 1/2\pi\sqrt{(2L_m + L_s)C_i}$. The second electric resonance f_2 is also associated with two identical branches, each with two L_s , one C_i , a coupling capacitor k_1C_i , and a coupling inductor k_2L_s at both ends, respectively, where $0 < k_1 < 1$ and $0 < k_2 < 1$ are the coupling efficient modeling the edge effect of two side interdigitals. Therefore, f_2 is calculated as $f_2 = 1/2\pi\sqrt{[(k_1C_i \times C_i)/(k_1C_i + C_i)](2 + k_2)L_s} = 1/2\pi\sqrt{2[k_1/(k_1 + 1)](k_2/2 + 1)L_sC_i}$. As for the third electric resonance f_3 , C_i and a half of L_s are responsible for it and thus quantitatively render as $f_3 = 1/2\pi\sqrt{L_s/2 \times C_i} = 1/2\pi\sqrt{L_sC_i/2}$. The origin of the multiband functionalities and correlative circuit models will be explained in depth

through the field distribution analysis performed in the next section.

Starting from the TL circuit model, the $ABCD$ matrix of the front TL element layer as well as the equivalent TL section comprising the composite effects of the substrate layer and magnetic resonances are formulated as

$$\begin{bmatrix} A_{\text{front}} & B_{\text{front}} \\ C_{\text{front}} & D_{\text{front}} \end{bmatrix} = \begin{bmatrix} 1 & 0 \\ 1/Z_{yi} & 1 \end{bmatrix}, \quad (1)$$

$$\begin{bmatrix} A_{\text{EqTL}} & B_{\text{EqTL}} \\ C_{\text{EqTL}} & D_{\text{EqTL}} \end{bmatrix} = \begin{bmatrix} \cos(kd_i) & jZ_{ci} \sin(kd_i) \\ j \sin(kd_i)/Z_{ci} & \cos(kd_i) \end{bmatrix}, \quad (2)$$

where k is equivalent wave vector of the TEM wave, and Z_{yi} is the impedance of the shunt branch at each resonant frequency f_i and is formulated as

$$Z_{y1} = 2j\omega L_m + 1/j\omega C_i + j\omega L_s + R_1, \quad (3)$$

$$Z_{y2} = \frac{k_1 + 1}{2j\omega k_1 C_i} + j\omega(k_2 + 2)L_s/2 + R_2/2, \quad (4)$$

$$Z_{y3} = j\omega L_s/8 + 1/4j\omega C_i + R_3/4. \quad (5)$$

By cascading the above two $ABCD$ matrices, the total matrix is calculated as

$$\begin{bmatrix} A & B \\ C & D \end{bmatrix} = \begin{bmatrix} A_{\text{front}} & B_{\text{front}} \\ C_{\text{front}} & D_{\text{front}} \end{bmatrix} \begin{bmatrix} A_{\text{EqTL}} & B_{\text{EqTL}} \\ C_{\text{EqTL}} & D_{\text{EqTL}} \end{bmatrix} = \begin{bmatrix} \cos(kd_i) & jZ_{ci} \sin(kd_i) \\ \cos(kd_i)/Z_{yi} + j \sin(kd_i)/Z_{ci} & jZ_{ci} \sin(kd_i)/Z_{yi} + \cos(kd_i) \end{bmatrix}. \quad (6)$$

The insertion of Eqs. (3)–(5) into Eq. (6) yields the total $ABCD$ matrix at three specific resonant frequencies. These analytic expressions are tedious and are not presented here. Then, the S parameters can be achieved from the $ABCD$ matrix by a transformation.³⁶ The circuit model analysis will be used for impedance matching and individual control over those multiresonant frequencies.

By tuning the LC values of these resonant tanks, a multiband absorber with an arbitrary frequency ratio can be engineered and nearly perfect absorptivity can be achieved. On the one hand, this can be physically implemented by appropriately tailoring the front electric resonators, a sandwiched substrate layer (thickness and dielectric constant) and background layer, to be equivalent so as to modulate the electric and magnetic resonances to coincide at the same frequency, thus enabling the absorber to be impedance matched to free space. On the other hand, there is no transmission ($S_{21} = 0$) through the absorber across the entire frequency range due to the shielding of the back metallic plate. In this case, both the electric and magnetic components of the incoming wave are almost completely absorbed. The design procedure is composed mainly of three steps. First, derive and adopt the equivalent circuit model in the circuit simulator advanced design system (ADS) to solve several groups of possible L , C , and R according to the target operating frequencies and other electrical characteristics such as bandwidth and absorptive efficiency. This can be carried out based on TL analysis and a refined optimization in ADS. Then select a prescription from the possible solutions such that the lumped elements can be readily accessed through standard printed circuit board (PCB) technology. Given these circuit elements, the physical layout is roughly synthesized according to the analytic equations.⁴² In the next process, the rough layout is extensively optimized in the EM simulator to maximize the absorption at specific frequencies.

Following the design procedure developed above, the final layout (with geometrical parameters presented in the caption

of Fig. 1) is engineered. For characterization, a single unit cell with a periodic boundary condition (PBC) assigned along the x and y directions and a Floquet port as the excitation is utilized to mimic infinite periodic arrays in Ansoft HFSS, a commercial full-wave finite-element-method (FEM) EM field solver. A commonly used F4B substrate with a dielectric constant of 2.65, a thickness of 3 mm, and a loss tangent of $\tan \delta = 0.002$ is employed for building. All metals in the absorber are copper with a conductivity of $\sigma = 5.8 \times 10^7$ S/m and a thickness of 0.036 mm. The relative wave impedance is retrieved as $z(\omega) = \sqrt{(1 + S_{11})^2 / (1 - S_{11})^2}$ (Ref. 26) and will be employed to evaluate the matching performances at the two closed interfaces.

Figure 2 depicts the simulated results of the proposed MA. At least three absorption peaks with absorptivities of 0.94, 0.92, and 0.923 are clearly observed at three well-separated frequencies $f_1 = 2.09$ GHz, $f_2 = 6.53$ GHz, and $f_3 = 10.3$ GHz, respectively. Higher absorption rates will be demonstrated by using a substrate with higher dielectric losses. At these frequencies, the real parts of $z(\omega)$ reach near unity, indicating $z = z(\omega)\eta_0 \approx \eta_0$, and thus good impedance matching at the interfaces. Notice that η_0 is the intrinsic impedance of the air. In addition, there is another smaller absorption peak (splitting) around the third peak which can be ascribed to the parasitic resonances of additional structures, and which will be discussed later in detail. The off-resonance absorption is very low and perfect absorption with a very narrow band only occurs near the resonant frequency. The frequency-sensitive absorption and the sharp notch response of the absorber show its promising potential in bolometric pixel elements and spectrum filters.

The most crucial characteristics should be the zero reflection phase (often defined as an artificial magnetic conductor) illustrated in Fig. 2(b) and the π phase change whenever the frequency was varied across each maximum reflection point (indicating a resonance behavior).⁴³ Therefore, multimagnetic resonances of a MTM which reflect the EM wave in phase at

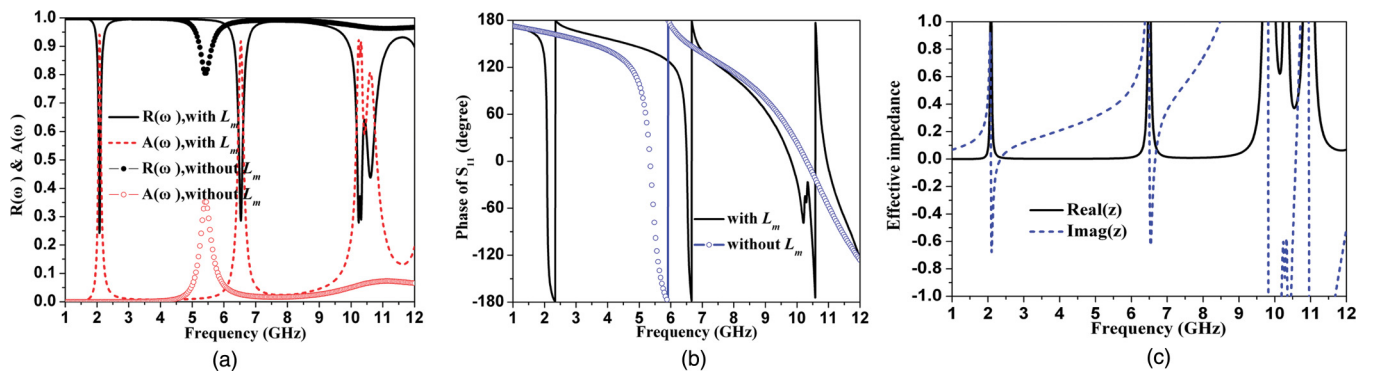


FIG. 2. (Color online) Numerical results of the proposed MA with and without the side meandered thin arms. (a) Magnitude of reflections and absorptions. (b) Reflection phase and (c) retrieved impedance.

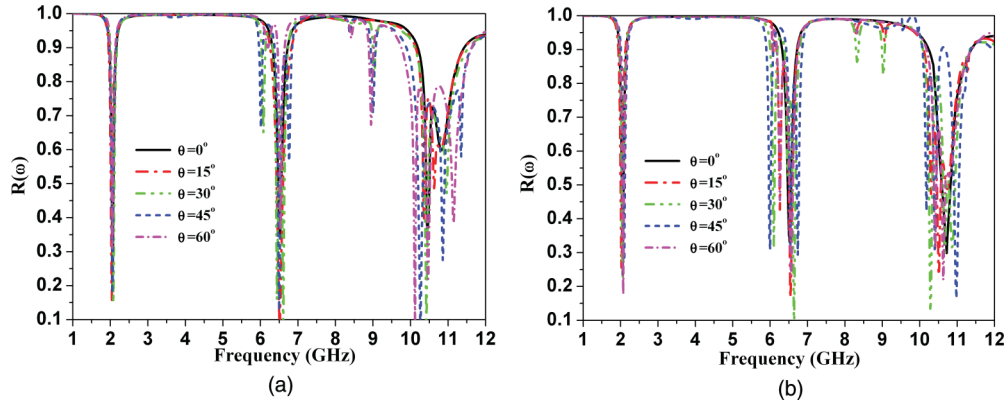


FIG. 3. (Color online) Angular independence of the reflectivity of the proposed MA for (a) TE and (b) TM wave radiation, respectively.

resonance are indicated by considering two aspects. Moreover, the zero phase regions coincide well with the regions where the imaginary parts of $z(\omega)$ approach zero in Fig. 2(c), illustrating a near-zero reflection. To preliminarily study the origin of the absorption peaks, we also simulate the absorber structure without the meandered arms and incorporate the results in Fig. 2(a) for comparison. Only two absorption peaks are clearly evidenced around f_2 and f_3 , revealing that the meandered thin lines contribute mainly to the disappeared f_1 while they have little effect on determining f_2 and f_3 . This enables f_1 to be independently adjusted. In addition to the slight frequency shift of f_2 and f_3 due to the composite response, the consequence of no meandered arms on the absorption peaks especially at f_3 indicates that the meandered thin lines essentially affect the impedance-matching performances over the entire frequency range.

Now that the absorber has been investigated under perpendicular incidence and x polarization, it is necessary to discuss the situations of large angles of oblique incidence with instable polarization states. Figure 3 shows the simulated reflection curves of the proposed MA against frequency for different oblique incident elevation angles (θ , defined as the angle between the wave vector and the normal) for both TE and TM polarizations, respectively. Following the figure, it is obvious that the dip in $R(\omega)$ maintains at less than 0.25 at f_1 and undergoes a negligible variation when θ varies from 0° to 60° in both the TE and TM cases. Nevertheless, the condition is slightly different at f_2 and f_3 because the reflection dips vary continuously and a series of ripples (additional dips) are exhibited around f_2 and f_3 . This is induced mainly because of the parasitic resonances of additional structures which enhance sharply as θ increases and can be evidenced from Fig. 7, and is partially due to the angle-dependent, higher-order resonances of the interdigitals and the calculation errors of the simulation engine in the analysis of such a refined structure. For verification, we have characterized the TL element under the same condition by substituting capacitive gaps for the interdigitals. Similarly, the ripples between the principle resonances are still exhibited, but the number and intensity seem to be reduced and weakened to some degree. Since the entire TL element contributes to the fundamental resonance, we hardly expect any such low parasitic resonances, thus accounting for an almost fixed fundamental resonance.

As for the latter two resonances, only the specific local region participates in resonating and any possible combination of the subrings and interdigitals may provide the parasitic resonances in the vicinity of f_2 and f_3 , thus accounting for the abundant ripples. Nevertheless, the original resonances are maintained all along in both the TE and TM cases no matter how much θ fluctuates, and the MA in all cases still exhibits a good performance with reflections of less than 0.4, which corresponds to an absorption of 84%.

The slight discrepancy between the TE and TM polarizations (the same for the measurement case) can be attributable to the fourfold rotational asymmetry of the meandered arms. This is especially true for the splitting in the third frequency absorption peak for EM wave excitation under normal incidence. For verification, the TL element with fourfold rotational symmetric but left-and-right asymmetric meandered arms is extensively characterized for both TE and TM excitation, respectively. Numerical results imply an almost identical frequency response between the two cases. As is expected, the resonant frequencies have suffered a serious blueshift, e.g., f_1 to 3.7 GHz, f_2 to 7.6 GHz, while f_3 to 12.9 GHz. For a comprehensive study, we also examine the sensitivity of the MA to the polarization states. The reflection characteristics under a normal incident planar TE wave with different polarizations (ϕ , defined as the angle between the E field and x axis) are plotted in Fig. 4. Following the figure, three evident reflection dips are obtained, which further confirms the multiband functionalities. Due to the high degree of fourfold rotational symmetry, the intensity of these reflection dips is nearly unchanged when ϕ changes from 0° to 90° . To sum up, the examination of Figs. 3 and 4 unambiguously demonstrates that the proposed triple-band MA operates stably with a wide range of incident angles and polarization states. The engineered multiband frequency selective performances and the insensitivity to the incident angles and polarization states which are not easily implemented through conventional bulk materials should be highlighted.

III. EXPERIMENTS AND DISCUSSIONS

For verification, a designed MA sample extending to 20×20 of the original unit cell shown in Fig. 1 is fabricated by means of standard PCB technology. The prototype with a

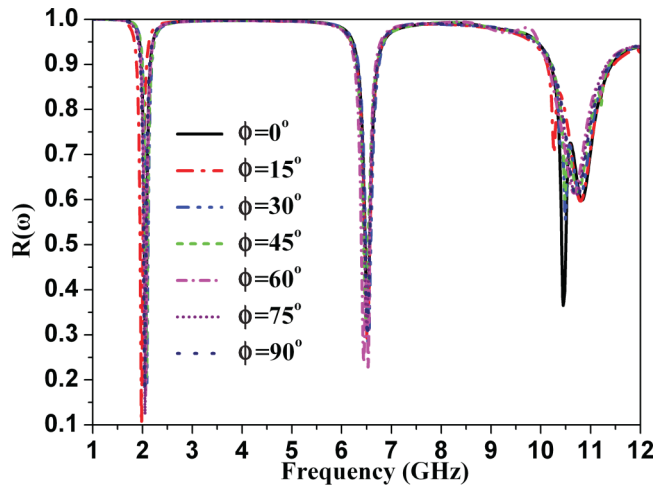


FIG. 4. (Color online) Polarization independence of the reflectivity of the proposed MA for TE wave excitation.

total footprint of $216 \times 216 \text{ mm}^2$ is built on the same F4B substrate (the thickness is evaluated as $\lambda_0/50$ at f_1) as that used in numerical simulations. Figure 5 illustrates the fabricated prototype and the experimental simulation setup in which a pair of double-ridged broadband horn antennas serving as the receiver and transmitter are connected to an Agilent N5230C vector network analyzer. The horn antennas, having a voltage standing wave ratio (VSWR) of <2 over a wide frequency range from 1 to 18 GHz, are placed on the same side of the sample. Pyramid absorbing materials in an anechoic chamber are adopted to enable the MA to be free of EM scattering from the complicated environment. The distance between the antennas and sample is kept to more than D^2/λ_0 to eliminate the near-field effects, where D is the largest transverse dimensions of the antenna's aperture. The network analyzer is calibrated, and the transmission and reflection coefficients are recorded using the free-space measurement method described in Ref. 24.

Figure 6 depicts the measured absorptive spectrum as a function of frequency for TE and TM radiation, respectively. For convenience of comparison, the simulated results for normal incidence are also provided. In both TE and TM

cases, the EM wave is obliquely incident with different angles ranging from 0° to 60° in steps of 20° . Under normal incidence, very obvious absorption peaks with measured values of 93.4%, 90.7%, and 91.56% are expected at three well-separated frequencies, $f_1 = 2.25 \text{ GHz}$, $f_2 = 6.6 \text{ GHz}$, and $f_3 = 10.32 \text{ GHz}$ in the TE mode case, whereas absorption rates of 90.6%, 93.8%, and 91.6% are expected at $f_1 = 2.18 \text{ GHz}$, $f_2 = 6.6 \text{ GHz}$, and $f_3 = 10.48 \text{ GHz}$ in the TM mode case. The slight frequency shift upwards in the measurement case is attributed to the tolerances that are inherent in the fabrication process. This is especially true for the proposed refined structure, e.g., the width and space of the interdigital fingers deviate from that in the simulation model by 0.05 mm. Further inspection indicates that the measured full width at half maximum (FWHM) is a little wider than that in the numerical case. This is especially true at f_1 and f_2 where the FWHM is obtained as 0.48 and 0.54 GHz for the TE mode while it is 0.42 and 0.45 GHz for the TM mode. This is induced by the shifted unignorable parasitic resonances of additional structures in the measurement case due to the implementation tolerances. Some of the parasitic resonances shift and follow tightly the principle resonances and thus facilitate the merged hybrid modes, and in turn the macroscopic wider bandwidth and the disappearance of high-frequency absorption peak splitting in experiments.

In a similar manner, the slightly larger off-resonance ripples with respect to those in simulation are mainly induced by enhanced parasitic resonances which are sensitive to the elevation angle, and are partially attributable to the measurement errors which are caused by the random noises of the imperfect experimental environment and the network analyzer. The discrepancy is particularly significant in the case of $\theta = 0^\circ$ because the normal incidence in the measurement with $\theta \approx 0^\circ$ is not exactly the ideal case in the simulation. Despite this, the simulated and measured results are desirably consistent. Moreover, the measured absorption peaks for both TE and TM radiations deteriorate some when θ arises. The gradually deteriorating magnetic flux (inefficient weak antiparallel currents) between the front and back metallic layers as θ increases²⁶ renders a dominant electric resonance and in turn an impedance mismatch. Therefore, the mostly reflected EM energy gives rise to a deteriorating

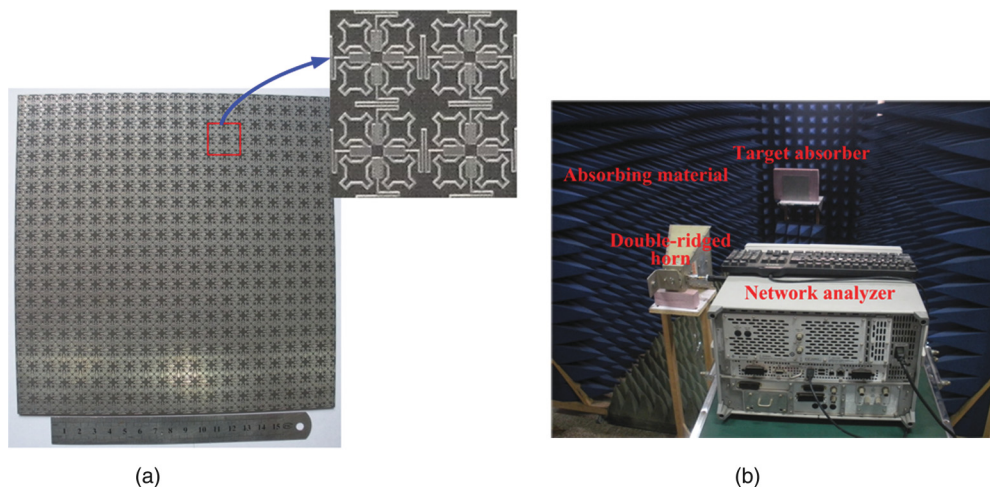


FIG. 5. (Color online) Photographs of the (a) fabricated prototype and (b) the experimental setup.

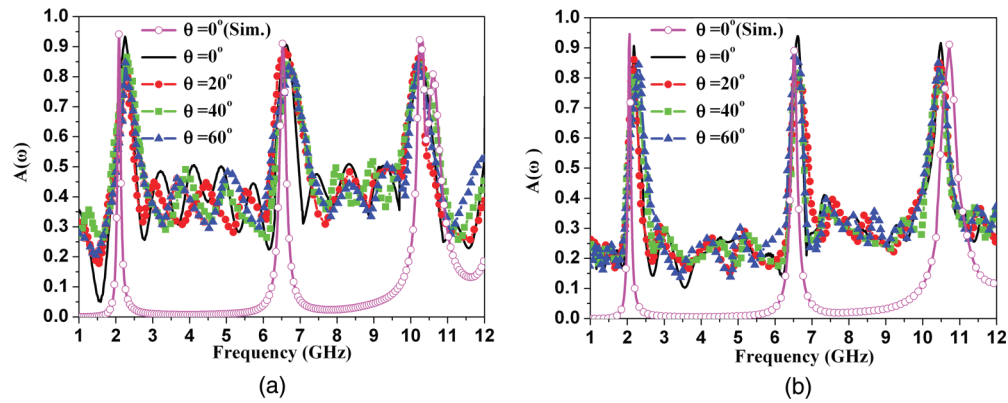


FIG. 6. (Color online) Measured absorption as a function of frequency for (a) TE and (b) TM radiation, respectively, at different angles of incidence.

absorptive efficiency for the large angle of incidence. Nevertheless, the absorption rates remain above 0.82 in all measurement cases. Therefore, a wide-angle incidence performance and a polarization insensitivity have been successfully validated.

To better understand the resonant mechanism and gain physical insight into the origin of the triple-band absorptions, in what follows we concentrate on performing two complementary analyses: a field-distribution analysis and circuit model analysis. Figure 7 delineates the surface current (a representation of magnetic energy density) and E -field (electric energy density) distributions obtained from HFSS. The arrow indicates the direction of flow while the color represents the intensity. Referring to the figure, it can be seen that three distinct resonant modes are evidently obtained from the surface current distribution. At f_1 , the oscillating linear currents driven by the y -polarized E field distribute homogeneously in the front layer, yielding a strong electric resonance through the two side meandered arms, four interdigitals, and subrings. The uniform current direction from the left-hand side to the right-hand side determines the series connection of the L_m , L_s , and C_i in the model shown in Fig. 1(b) while the antiparallel currents in the top and bottom half ring render a parallel connection of two subcircuits each with a series tank of L_s and C_i . The formed electric resonator couples strongly to the E field around f_1 . The uniform currents along the y direction in the whole ground are antiparallel to those exhibited in the TL element, and the resulting current loop is driven by the H field, resulting in a strong magnetic resonance similar to the so-called fishnet and paired nanorod structure.⁴⁴ Following Fig. 7(a), the E field is mostly localized within the four interdigitals and thus most of the power is lost due to a high confinement of energy.

At f_2 , the currents in the meandered lines and fractal rings are antiparallel, illustrating that the meandered lines no longer contribute to the electric resonance. In a similar manner, the subrings and interdigitals in the top and bottom regions of the TL element fashion two parallelly connected subcircuits, each coupling strongly to the E field. This can be further validated by the highly concentrated E field in the two top and bottom interdigitals and the negligible weak E field presented in the two left and right interdigitals. Despite this, the high electric

energy density in the four corners indicates strong electric coupling between the adjacent interdigitals due to the close arrangement. On the left-hand side of the TL element, the ring indirectly connects the meandered line through an edge capacitive effect of the interdigital, whereas they are directly connected through a side interdigital finger (edge inductive effect) on the right-hand side. The coefficient k_1 measures the capacitive coupling strength and is dependent on the length and number of fingers, whereas k_2 models the inductive effect and is dependent on L_s . Both k_1 and k_2 can be monitored for an independent manipulation of f_2 . The antiparallel currents formed in the top and bottom region between the TL element and ground give rise to the corresponding magnetic resonance. At for f_3 , the surface currents in each subring are interrupted at the middle point and they are in a reverse direction, with those in the adjacent subring forming four parallel resonant tanks, each formed by $L_s/2$ and C_i . The electric resonators in these four specific regions impinge strongly on the electric components of the EM wave, enabling the electric energy to be mainly confined in the four interdigitals. Meanwhile, the reversed currents formed in the specific region between the front and back layers facilitate the third magnetic resonance.

To sum up, the absorber is capable of trapping the EM wave (both electric and magnetic field components) in some specific locations due to the self-similar nature of the fractals.⁴³ The energy is significantly reinforced, then converted into thermal energy, and subsequently completely consumed, leading to a strong absorption. Moreover, the currents and E -field intensity in the residual region of the TL element are not negligible with respect to those in the resonant region at the latter two principle resonances, indicating evidence of the parasitic resonances of the additional structures.

To further validate the resonant mechanism, we have performed both a theoretical analysis and a quantitative circuit analysis based on previous results. For this purpose, L_s is roughly evaluated as $k_3 = 0.18$ times of L_m according to Ref. 42. k_1 and k_2 can be roughly assessed through the intensity of the E field and are obtained as $k_1 = k_2 = 0.8$, respectively, in this particular design. Given $f_3 = 10.3$ GHz, f_1 is immediately obtained as 6.529 GHz, which is quantitatively very similar to 6.3 GHz obtained from the EM full-wave simulation.

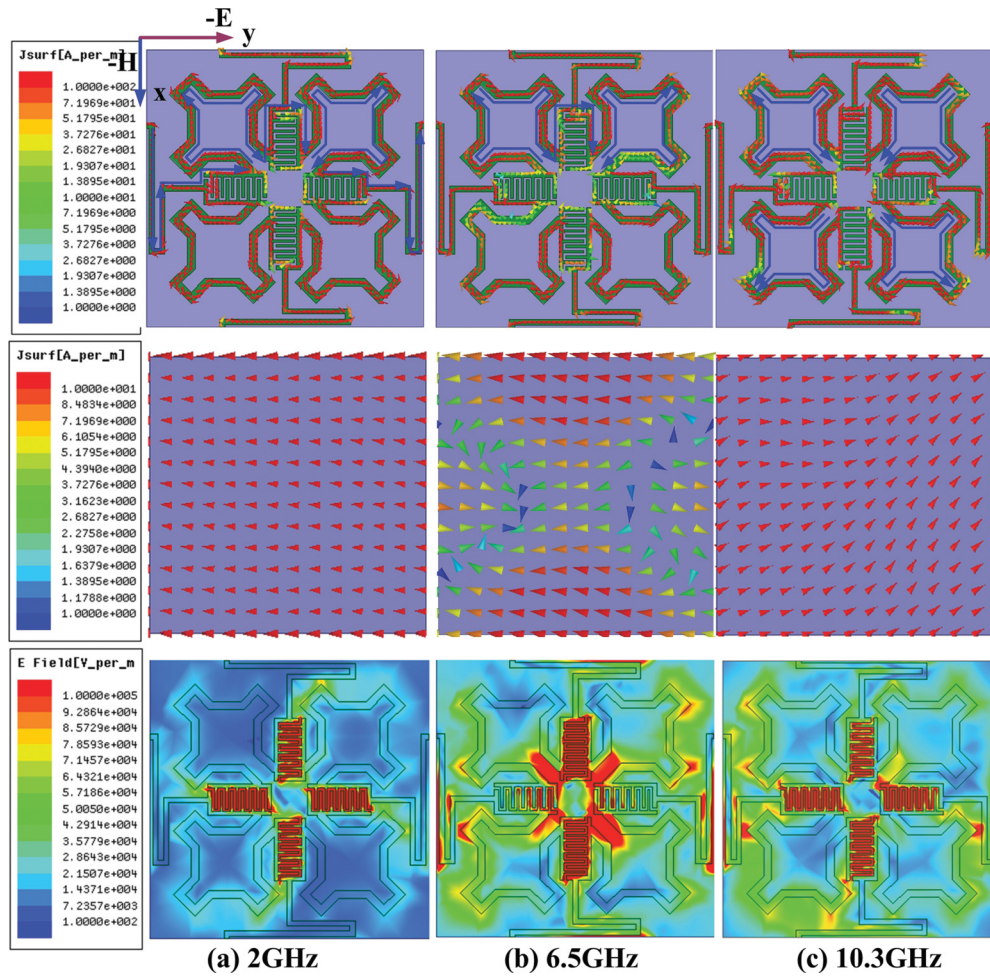


FIG. 7. (Color online) Surface current and E -field distributions of the proposed MTM triple-band absorber at three resonant frequencies: (a) $f_1 = 2$ GHz, (b) $f_2 = 6.5$ GHz, and (c) $f_3 = 10.3$ GHz, respectively. The top and middle rows are the current distributions on the front metallic pattern and the background, respectively, while the bottom row is the E -field distributions on the front layer.

Providing k_1, k_2, k_3 , and f_2, f_1 is straightforwardly computed as $f_1 = 2.093$ GHz, which is quantitatively almost the same as 2.09 GHz. For comprehensive verification, Fig. 8 compares the reflection coefficients of the MA between the full-wave simulation and circuit model analysis based on TL theory in both the resonant and off-resonance regions. To investigate the influence of the ohmic losses on the reflection performances, the MAs with $0.5R_1, 0.5R_2$, and $0.5R_3$ (red curve) and with $4R_1, 4R_2$, and $4R_3$ (green curve) are analyzed and the corresponding reflection curves are also compared. As is shown, a desirable agreement in resonant frequency is notably observed. All triple-band reflection responses indicate that the FWHM can be significantly enhanced when ohmic loss is increased, coinciding well with the conclusion drawn for a single-band TL analysis.³⁶ Therefore, the analysis has unambiguously validated the rationality of the circuit model, which affords us a good guideline for individual control over these resonances, e.g., f_1 can be exclusively controlled by the ratio of meandered lines to the fractal ring while the coupling effect enables independent control over f_2 .

Finally, we have investigated the origin of the loss to better understand the absorption mechanism by comparing four cases: (a) copper ($\sigma = 5.8 \times 10^7$ S/m) and a larger loss

substrate ($\tan \delta = 0.02$); (b) copper and a lossless substrate ($\tan \delta = 0$); (c) PEC (perfect electric conductor) and a large

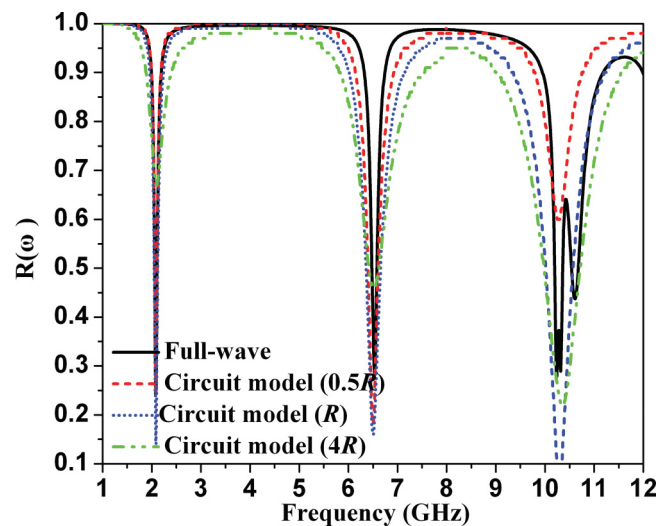


FIG. 8. (Color online) Comparison of the calculated reflection coefficients between full-wave simulation and circuit model analysis.

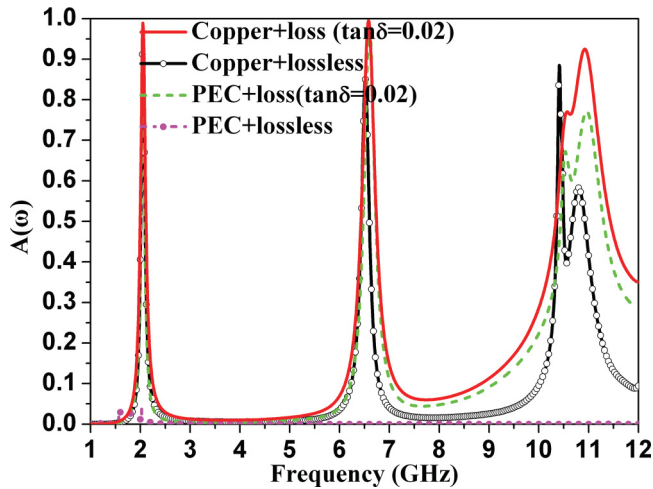


FIG. 9. (Color online) Calculation of absorptivity as a function of frequency for different material properties of metallic layers and dielectrics.

loss substrate; and (d) PEC and a lossless substrate. Including the practical condition in the experiment, there are a total of five conditions. Figure 9 compares the absorption spectrum under these different cases. As is shown, the MA in case (a) affords the largest absorption peaks, while the absorption peaks in cases (b) and (c) are reduced slightly, indicating that without ohmic loss in metals or dielectric loss in the substrate the MA can still work well. In contrast, the MA in case (d) is almost without absorption, implying that both the ohmic and dielectric losses contribute to the absorption rates. Also, we find that the contribution of dielectric loss to absorption at f_2 is

more significant than that of the ohmic loss, while the ohmic loss plays a more important role in contributing absorption at f_1 and f_3 . This is different from the conclusion drawn in Ref. 27. Moreover, the absorption peaks have been increased to 0.988, 0.994, and 0.925 by increasing $\tan \delta$ from 0.002 to 0.02 with the residual parameters fixed, illustrating that a high dielectric loss is beneficial for a high absorption rate.¹⁶

In summary, we have presented the design, fabrication, and measurement of a triple-band MA enhanced from a MTM TL concept. The fractal perturbation is introduced to overcome the challenge of increasing the inductors and capacitors in a limited volume, leading to a more homogenized material and a subwavelength resonator. The physical mechanism for the multiresonances is comprehensively studied, showing that different LC resonant circuits formed in the specific local area are responsible for the abnormal phenomena. The most important aspect is that the frequency ratio between these resonances can be arbitrarily tuned behind a sophisticated design procedure that has been derived. Due to the geometry scalability, this triple-band MA could be realized over much of the EM spectrum with nearly perfect absorption. A terahertz absorber using this concept is now under investigation.

ACKNOWLEDGMENTS

This work is supported by the National Natural Science Foundation of China under Grant No. 60971118 and the 973 Project of Science and Technology Ministry under Grant No. 2009CB613306. It is also supported by the Innovation Foundation for Postgraduate's Dissertation of Air Force Engineering University under Grant No. DY12101.

¹N. I. Landy, S. Sajuyigbe, J. J. Mock, D. R. Smith, and W. J. Padilla, *Phys. Rev. Lett.* **100**, 207402 (2008).

²B. Zhu, Z. Wang, C. Huang, Y. Feng, J. Zhao, and T. Jiang, *Prog. Electromagn. Res.* **101**, 231 (2010).

³B. N. Wang, T. Koschny, and C. M. Soukoulis, *Phys. Rev. B* **80**, 033108 (2009).

⁴F. Costa, A. Monorchio, and G. Manara, *IEEE Trans. Antennas Propag.* **58**, 1551 (2010).

⁵Y. Z. Cheng and H. L. Yang, *J. Appl. Phys.* **108**, 034906 (2010).

⁶Y. Avitzour, Y. A. Urzhumov, and G. Shvets, *Phys. Rev. B* **79**, 045131 (2009).

⁷N. Liu, M. Mesch, T. Weiss, M. Hentschel, and H. Giessen, *Nano Lett.* **10**, 2342 (2010).

⁸J. A. Mason, S. Smith, and D. Wasserman, *Appl. Phys. Lett.* **98**, 241105 (2011).

⁹W. R. Zhu and X. P. Zhao, *J. Opt. Soc. Am. B* **26**, 2382 (2009).

¹⁰J. M. Hao, J. Wang, X. L. Liu, W. J. Padilla, L. Zhou, and M. Qiu, *Appl. Phys. Lett.* **96**, 251104 (2010).

¹¹W. R. Zhu, X. P. Zhao, B. Y. Gong, L. H. Liu, and B. Su, *Appl. Phys. A* **102**, 147 (2011).

¹²H. Tao, N. I. Landy, C. M. Bingham, X. Zhang, R. D. Averitt, and W. J. Padilla, *Opt. Express* **16**, 7181 (2008).

¹³H. Tao, C. M. Bingham, A. C. Strikwerda, D. Pilon, D. Shrekenhamer, N. I. Landy, K. Fan, X. Zhang, W. J. Padilla, and R. D. Averitt, *Phys. Rev. B* **78**, 241103 (2008).

¹⁴N. I. Landy, C. M. Bingham, T. Tyler, N. Jokerst, D. R. Smith, and W. J. Padilla, *Phys. Rev. B* **79**, 125104 (2009).

¹⁵Q. Y. Wen, H. W. Zhang, Y. S. Xie, Q. H. Yang, and Y. L. Liu, *Appl. Phys. Lett.* **95**, 241111 (2009).

¹⁶H. Tao, C. M. Bingham, D. Pilon, K. B. Fan, A. C. Strikwerda, D. Shrekenhamer, W. J. Padilla, X. Zhang, and R. D. Averitt, *J. Phys. D* **43**, 225102 (2010).

¹⁷P. K. Singh, K. A. Korolev, M. N. Afsar, and S. Sonkusale, *Appl. Phys. Lett.* **99**, 264101 (2011).

¹⁸Y. Ma, Q. Chen, J. Grant, S. C. Saha, A. Khalid, and D. R. S. Cumming, *Opt. Lett.* **36**, 945 (2011).

¹⁹X. J. He, Y. Wang, J. M. Wang, T. L. Gui, and Q. Wu, *Prog. Electromagn. Res.* **115**, 381 (2011).

²⁰Z. H. Jiang, S. Yun, F. Toor, D. H. Werner, and T. S. Mayer, *ACS Nano* **5**, 4641 (2011).

²¹B. Zhang, Y. Zhao, Q. Hao, B. Kiraly, I.-C. Khoo, S. Chen, and T. J. Huang, *Opt. Express* **19**, 15221 (2011).

²²H. M. Lee and J. C. Wu, *J. Phys. D* **45**, 205101 (2012).

²³X. P. Shen, T. J. Cui, and J. X. Ye, *Acta Phys. Sin.* **61**, 058101 (2012) (in Chinese).

²⁴M. H. Li, H. L. Yang, X. W. Hou, Y. Tian, and D. Y. Hou, *Prog. Electromagn. Res.* **108**, 37 (2010).

²⁵H. Li, L. H. Yuan, B. Zhou, X. P. Shen, Q. Cheng, and T. J. Cui, *J. Appl. Phys.* **110**, 014909 (2011).

- ²⁶Q. W. Ye, Y. Liu, H. Lin, M. H. Li, and H. L. Yang, *Appl. Phys. A* **107**, 155 (2012).
- ²⁷L. Li, Y. Yang, and C. H. Liang, *J. Appl. Phys.* **110**, 063702 (2011).
- ²⁸L. Huang and H. Chen, *Prog. Electromagn. Res.* **113**, 103 (2011).
- ²⁹C. Gu, S. B. Qu, Z. B. Pei, Z. Xu, J. Liu, and W. Gu, *Chin. Phys. B* **20**, 017801 (2011).
- ³⁰Y. X. Zhang, S. Qiao, T. Zhao, W. Ling, and S. Liu, *Prog. Electromagn. Res.* **125**, 21 (2012).
- ³¹A. Noor and Z. Hu, *IET Microwaves Antennas Propag.* **4**, 667 (2010).
- ³²F. Ding, Y. X. Cui, X. C. Ge, Y. Jin, and S. L. He, *Appl. Phys. Lett.* **100**, 103506 (2012).
- ³³Y. Q. Pang, H. F. Cheng, Y. J. Zhou, Z. G. Li, and J. Wang, *Opt. Express* **20**, 12515 (2012).
- ³⁴L. K. Sun, H. F. Cheng, Y. J. Zhou, and J. Wang, *Opt. Express* **20**, 4675 (2012).
- ³⁵C. H. Wu and G. Shvets, *Opt. Lett.* **37**, 308 (2012).
- ³⁶Q. Y. Wen, Y. S. Xie, H. W. Zhang, Q. H. Yang, Y. X. Li, and Y. L. Liu, *Opt. Express* **17**, 20256 (2009).
- ³⁷A. K. Iyer and G. V. Eleftheriades, *J. Opt. Soc. Am. B* **23**, 553 (2006).
- ³⁸H.-T. Chen, J. Zhou, J. F. O'Hara, F. Chen, A. K. Azad, and A. J. Taylor, *Phys. Rev. Lett.* **105**, 073901 (2010).
- ³⁹D. Y. Shchegolkov, A. K. Azad, J. F. O'Hara, and E. I. Simakov, *Phys. Rev. B* **82**, 205117 (2010).
- ⁴⁰H.-T. Chen, *Opt. Express* **20**, 7165 (2012).
- ⁴¹H. Ghali and T. A. Moselhy, *IEEE Trans. Microwave Theory Tech.* **52**, 2513 (2004).
- ⁴²I. Bahl and P. Bhartia, *Microwave Solid State Circuit Design* (Wiley, Hoboken, NJ, 2003).
- ⁴³W. Wen, L. Zhou, J. Li, W. Ge, C. T. Chan, and P. Sheng, *Phys. Rev. Lett.* **89**, 223901 (2002).
- ⁴⁴J. F. Zhou, L. Zhang, G. Tuttle, T. Koschny, and C. M. Soukoulis, *Phys. Rev. B* **73**, 041101 (2006).